Article:
Barrows, A.T., Lilliu, S., Pearson, A.J. et al. (2016) Monitoring the Formation of a CH<inf>3</inf>NH<inf>3</inf>PbI<inf>3-</inf><inf>x</inf>Cl<inf>x</inf> Perovskite during Thermal Annealing Using X-Ray Scattering. Advanced Functional Materials, 26 (27). pp. 4934-4942. ISSN: 1616-301X

https://doi.org/10.1002/adfm.201601309

ADVANCED FUNCTIONAL MATERIALS
www.afm-journal.de

Monitoring the Formation of a $CH_3NH_3PbI_{3-x}Cl_x$ Perovskite during Thermal Annealing Using X-Ray Scattering

*Alexander T. Barrows, Samuele Lilliu, Andrew J. Pearson, David Babonneau, Alan D. F. Dunbar, and David G. Lidzey**

Grazing incidence wide and small angle X-ray scattering (GIWAXS and GISAXS) measurements have been used to study the crystallization kinetics of the organolead halide perovskite $CH_3NH_3PbI_{3-x}Cl_x$ during thermal annealing. In situ GIWAXS measurements recorded during annealing are used to characterize and quantify the transition from a crystalline precursor to the perovskite structure. In situ GISAXS measurements indicate an evolution of crystallite sizes during annealing, with the number of crystallites having sizes between 30 and 400 nm increasing through the annealing process. Using ex situ scanning electron microscopy, this evolution in length scales is confirmed and a concurrent increase in film surface coverage is observed, a parameter crucial for efficient solar cell performance. A series of photovoltaic devices are then fabricated in which perovskite films have been annealed for different times, and variations in device performance are explained on the basis of X-ray scattering measurements.

1. Introduction

In recent years organometal halide perovskites have become the hot topic of solar cell research within the academic community. These materials were first explored in solar cells as recently as 2006[1,2] and in solid-state solar cells as recently as 2012,[3,4] and have since seen an unprecedented increase in power conversion efficiency (PCE). Building upon the initial results through device optimization and materials purification, perovskite solar cells (PSCs) can now exhibit unstabilized PCEs in excess of 20%, significantly outperforming competing classes of next generation photovoltaics.[5] In parallel with these developments, there has been a significant improvement in the understanding of the physical properties of these materials. This not only includes the operating principles of different PSC architectures, but also fabrication methods compatible with large scale and low cost manufacturing.[6–8] Combining these factors, it is clear that organometal halide perovskites have significant promise as a family of semiconductors for solar energy harvesting in commercial applications.

To fabricate PSCs, a range of techniques have been employed for the deposition and formation of the light harvesting perovskite layer. These include vacuum deposition of the perovskite components[9] and solution deposition of perovskite precursor inks.[10] Two approaches can be adopted for solution deposition, commonly referred to as either "one-step" or "two-step" processing. In the one-step process, blends of a lead salt and an organic component (e.g., lead (II) chloride and methylammonium iodide) are dissolved in a common solvent such as dimethylformamide (DMF) or dimethyl sulfoxide and cast to form a thin film, typically having a thickness of a few hundred nanometers. Following solution casting, thermal annealing is then used to create the perovskite structure. The simplicity of this approach has afforded the straightforward transfer of one-step processing from small area deposition methods (e.g., spin-casting) to techniques that are compatible with large-area substrates such as spray-coating[6,11] and inkjet printing.[12] In contrast, in the two-step process, a perovskite film is formed via the initial deposition of a film of a lead salt followed by its exposure to an organic halide, either in a vapor or a solution phase.[8,13–16] Because both one-step and two-step procedures have been used to produce high performance PSCs,[16–22] both continue to be investigated in order to understand the basic mechanisms of perovskite formation and thus identify routes for further improvements in PSC efficiency.

Here, we characterize the formation of $CH_3NH_3PbI_{3-x}Cl_x$ via thermal annealing in air of a precursor film prepared using the one-step procedure. A combination of 2D grazing incidence

A. T. Barrows, Dr. S. Lilliu, Prof. D. G. Lidzey
Department of Physics and Astronomy
University of Sheffield
Hicks Building
Hounsfield Road, Sheffield S3 7RH, UK
E-mail: d.g.lidzey@sheffield.ac.uk
Dr. A. J. Pearson
Cavendish Laboratory
University of Cambridge
19 JJ Thomson Avenue, Cambridge CB3 0HE, UK
Dr. D. Babonneau
Institut Pprime
Département Physique et Mécanique des Matériaux
UPR 3346 CNRS
Université de Poitiers, SP2MI
11 Boulevard Marie et Pierre Curie, BP 3017986962
Futuroscope Chasseneuil Cedex, France
Dr. A. D. F. Dunbar
Department of Chemical and Biological Engineering
The University of Sheffield
Sir Robert Hadfield Building
Mappin St, Sheffield S1 3JD, UK

DOI: 10.1002/adfm.201601309

wide angle X-ray scattering (GIWAXS) and small angle X-ray scattering (GISAXS) measurements are used to track the crystallization of the perovskite film in situ. We note that the first use of GISAXS for the investigation of organometal halide perovskite films was made by Schlipf et al., who undertook a detailed investigation of two-step fabrication of planar $CH_3NH_3PbI_{3-x}Cl_x$ films and concluded that the length scales present in the final perovskite films were very similar to those observed in the initial PbI_2 film, suggesting that control of PbI_2 morphology is critical in controlling the morphology of the final perovskite film.[27] Liao et al. have also used ex situ GISAXS to investigate $CH_3NH_3PbI_3$ deposited via both one-step and two-step methods.[22] Here, evidence of pores was observed within the perovskite crystal grains, with such pores being subsequently filled by the electron or hole transporting material that was deposited onto the perovskite film. The perovskite devices fabricated in this study using a one-step process, however, had a low average PCE of only 2.2% as a result of poor surface coverage. In our work, we use in situ GISAXS measurements to explore perovskite materials that were deposited from a one-step process. The inverted, planar-architecture PSC devices made from our films achieve an average PCE of 12.2%. The in situ GISAXS measurements show an evolution of the size distribution of the perovskite crystallites during annealing of a precursor film, which is confirmed using ex situ scanning electron microscopy (SEM). We also apply a kinetic model to GIWAXS measurements on representative perovskite films to extract the activation energy for the formation of $CH_3NH_3PbI_{3-x}Cl_x$. Our work advances upon existing X-ray diffraction measurements on $CH_3NH_3PbI_{3-x}Cl_x$ and $CH_3NH_3PbI_3$ films[22–27] by providing detailed access to the dynamics of structural changes during film processing over three orders of magnitude in length scale.

2. Results and Discussion

2.1. In Situ GIWAXS

We first consider the evolution in film structure as characterized by in situ GIWAXS measurements performed on $CH_3NH_3PbI_{3-x}Cl_x$ films having a thickness of ≈400 nm. An MAI:$PbCl_2$ precursor ink (3:1 molar ratio) was deposited via spin-coating under ambient conditions (relative humidity, RH ≈ 40%–45%) onto Si substrates with a native SiO_2 layer coated with PEDOT:PSS to replicate the hole transport layer employed in our solar cells. After spin-coating, the precursor films were immediately transferred to a sample chamber for GIWAXS measurement and a single diffraction pattern was recorded at room temperature as a reference (t = 0 min). Films were subsequently heated in situ and annealed under isothermal conditions for a period of up to 3 h (see the Experimental Section).

Figure 1 shows a summary of the in situ GIWAXS data recorded during thermal annealing at 80 °C, a temperature at which resultant perovskite films lead to high performance solar cells (see Figure S8, Supporting Information). In Figure 1a,b (corresponding to t = 0 and 8 min respectively), it can be seen that the GIWAXS pattern is characterized by a large number of rings having a nonuniform intensity distribution in the azimuthal direction, indicative of a polycrystalline sample with some degree of crystallite orientation present. In Figure 1f, we plot the radial line profiles recorded at different points within the annealing process. As reported previously, we observe an unidentified, ordered, crystalline precursor phase during the early stages of annealing as evidenced by the rings located around $q \approx 0.45$ Å^{-1} and ≈0.8–0.9 Å^{-1}.[24,26] In line with previous reports, the ring at $q \approx 1$ Å^{-1} is attributed to the (110) and (002) planes of the tetragonal $CH_3NH_3PbI_{3-x}Cl_x$ perovskite.[4,9,25,28] It is apparent that this broad feature having maximum intensity at $q \approx 1.00$ Å^{-1} is actually composed of a number of narrower peaks, with peaks evident at both q = 1.00 and 1.05 Å^{-1}. This observation is consistent with the existence of a series of crystallites within the film having different lattice constants, perhaps due to the coexistence of multiple perovskite phases.[29,30] In fact, the diffraction rings observed in Figure 1a–e are made up of a large number of diffraction spots having slightly different q values. We note both that the material commonly denoted as $CH_3NH_3PbI_{3-x}Cl_x$ actually appears to be structurally similar to $CH_3NH_3PbI_3$, and that due to the temperature during the GIWAXS measurements (80 °C) being above the reported transition temperature for these materials from the tetragonal to cubic structure (≈55 °C), the diffraction ring at $q \approx 1$ Å^{-1} may in fact be attributable to the (100) peak of the cubic structure.[30–32] Whilst it is tempting to estimate domain size from analysis of peak widths, we believe that this process would likely be in error due to (i) differences in lattice constant of the various domains, and (ii) peak broadening effects due to the integration of the scattering signal over the angular range χ = 0° to χ = 90°.

Due to the relatively high ambient humidity in the experimental environment (RH ≈ 40%–45%), it was found that the yellow precursor film rapidly became grey during spin-coating. We attribute this to the formation of a perovskite upon exposure of the rapidly cooling precursor film to ambient atmosphere, as has been reported previously in the Supporting Information of ref. [26]. Upon heating the film returned to the bright yellow color whilst, as can be seen in Figure 1a,b,f, the intensity of the $q \approx 1.00$ Å^{-1} diffraction ring dropped to a minimum at t = 8 min and the intensity of the precursor peaks increased, indicating a return to the precursor phase. As the thermal anneal proceeded, the intensity of the $q \approx 1.00$ Å^{-1} diffraction ring increased, reaching a maximum integrated intensity at t = 117 min. This is accompanied by a simultaneous reduction in the intensity of the peaks attributed to the crystalline precursor phase, indicating a transformation of the precursor into $CH_3NH_3PbI_{3-x}Cl_x$. In Figure 1g it can be clearly seen that the precursor peak at ≈0.45 Å^{-1} has all but disappeared by ≈115 min, an observation that is also seen in the radial profile of the diffraction image at 117 min shown in Figure 1f. At the longest annealing times (164 min) a new peak emerges at $q \approx 0.9$ Å^{-1}, attributable to PbI_2.[24,33,34] Due to the overlap of this peak with the precursor peaks however, it is difficult to quantify the exact time at which it emerges. We find however that the growth of this feature is accompanied by a relative reduction in intensity of the peak at $q \approx 1$ Å^{-1}, indicating a decomposition of the $CH_3NH_3PbI_{3-x}Cl_x$ (this effect is particularly clear when annealing at higher temperatures as shown in Figures S1 and S2 in the Supporting Information). The relatively prompt onset of perovskite decomposition observed here is likely attributable to the high relative

DOI: 10.1002/adfm.201601309

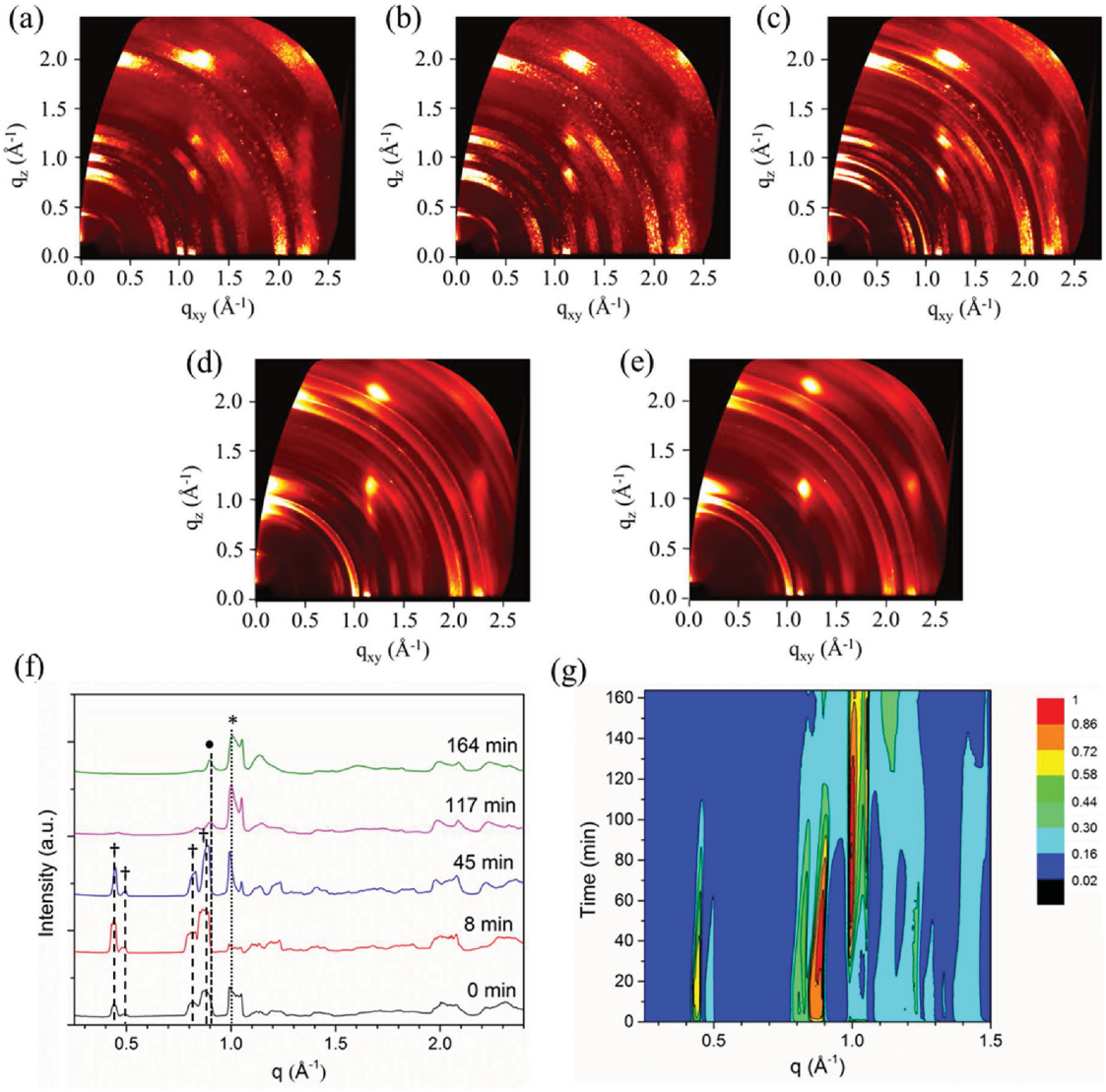

Figure 1. 2D GIWAXS patterns recorded during an anneal at 80 °C. Images are presented at a) $t = 0$, b) $t = 8$ min (corresponding to the lowest integrated intensity of the $q \approx 1$ Å^{-1} perovskite peak), c) $t = 45$ min (corresponding to 50% of the maximum integrated intensity of this peak), d) $t = 117$ min (the maximum integrated intensity of the $q \approx 1$ Å^{-1} peak), and e) $t = 164$ min (the end of the annealing experiment). f) Azimuthally integrated intensity profiles determined at these times; vertical lines indicate peaks associated with perovskite (*), precursor phase (†), and PbI_2 (•). g) The evolution of the GIWAXS profile through the annealing process as a contour plot of (normalized) azimuthally integrated intensity.

humidity (RH ≈ 40%–45%) during the experiment.[24] Although we cannot rule out possible beam damage accelerating this decomposition, it is notable that similar experiments performed under a dry nitrogen atmosphere do not lead to such rapid degradation, implying that humidity and/or oxygen are likely the principal cause of the observed decomposition under ambient conditions (see Figure S4, Supporting Information).

By comparing Figure 1(a) and 1(d) it can be seen that some of the preferential crystallite orientation detected at early times persists throughout the annealing process. To determine the extent of this observation, we plot azimuthal profiles of the X-ray scattering intensity for the feature at $q \approx 1$ Å^{-1} in **Figure 2** (i.e., intensity vs azimuth χ, where χ is the azimuth of q_z and q_{xy} in scattering vector polar coordinates with $\chi = 0°$ at positive q_z and $\chi = 90°$ at positive q_{xy}).[35] Data is presented at various times during the annealing process, with each trace normalized to its maximum intensity (at $\chi \approx 6°$). We find that scattering intensity is initially greatest close to $\chi = 0°$, indicating preferential orientation of the (110) and (002) perovskite planes in the out-of-plane direction. Note however that a relatively small population of $CH_3NH_3PbI_{3-x}Cl_x$ crystallites have in-plane orientation, as evidenced by the intensity of X-ray scatter close to $\chi = 90°$. It can be seen that this preferential orientation persists during annealing, although X-ray scattering intensity increases slightly at intermediate angles of χ, implying that annealing drives a somewhat broader distribution of crystallite orientation relative to the structures formed during the preparation of the precursor film. Preferential out-of-plane orientation of the (110) and (002) diffraction peak has previously been observed in planar $CH_3NH_3PbI_3$ films on compact TiO_2.[36] Very recently it has been reported that

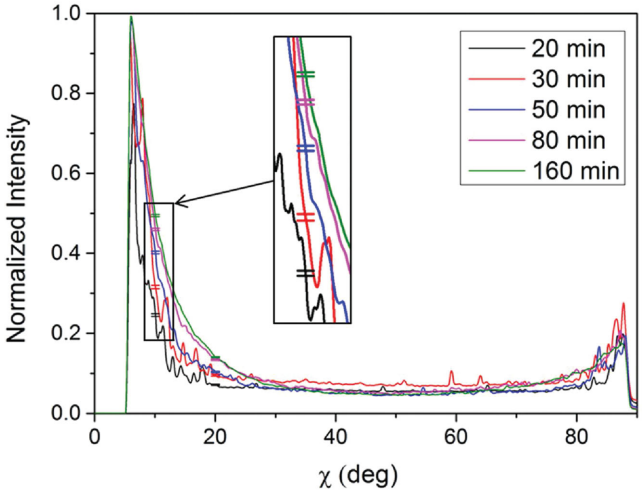

Figure 2. Azimuthal profiles for the $q \approx 1$ Å^{-1} diffraction peak during annealing at 80 °C. A 5 point moving average has been used in order to smooth the data. Error bars determined on the basis of Poissonian statistics are shown at $\chi = 10°$ and 20°; the inset shows an expanded view of the error bars at $\chi = 10°$.

planar films prepared in a similar manner to that reported here had strong preferential out-of-plane orientation and attained high performance in a PSC.[37] In contrast, preferential in-plane orientation has been observed for $CH_3NH_3PbI_{3-x}Cl_x$ films fabricated on mesoporous Al_2O_3 scaffolds.[38]

Following the approach of Moore et al.,[25] we determine the activation energy E_A for the formation of $CH_3NH_3PbI_{3-x}Cl_x$ following the isothermal annealing of an MAI:$PbCl_2$ precursor film. Here, films were annealed at three different temperatures (80 °C, 90 °C, and 110 °C) with relative changes in integrated intensity of the $q \approx 1$ Å^{-1} peak on the GIWAXS data used to gauge the fraction of material transformed into the perovskite structure. Full details are provided in the Supporting Information. We find $E_A = (85 \pm 9)$ kJ mol^{-1}, a value in good agreement with the (86 ± 6) kJ mol^{-1} reported by Moore et al. for the same precursor system. Note that this activation energy corresponds to the entire transformation from precursor to perovskite and does not decouple activation energies relating to nucleation and growth modes.

2.2. In Situ GISAXS and Ex Situ SEM

We now discuss the evolution in film structure during thermal annealing as characterized through in situ GISAXS measurements. These measurements complement the wide angle scattering dataset by characterizing the sample at q values as low as 10^{-3} Å^{-1} which in real space corresponds to length scales as large as 400 nm, a size that is potentially commensurate with that of individual perovskite grains.[39–43] Measurements were performed under nominally identical conditions to the GIWAXS measurements, although the relative humidity was slightly higher (RH ≈ 45%–50% as opposed to 40%–45% during the GIWAXS experiments). Sample preparation followed the same procedures as used in the GIWAXS experiment described above, except that the spin-coated precursor samples were directly placed onto a preheated hotplate rather than being ramped from room temperature to the desired anneal temperature. Full technical details are provided in the Experimental Section.

Typical 2D GISAXS patterns collected at $t = 0$ and 120 min are displayed in **Figure 3**e,f, respectively. Line profiles in q_y were taken at the Yoneda Peak for each image.[44] Owing to a slight shading from the beam-stop, visible on the right-hand side of Figure 3e,f, all line profiles presented are taken from the left side of the images. Quantitative analysis of GISAXS measurements has been undertaken using the distorted wave born approximation to simulate scattering from periodic features in the film under investigation. Unfortunately, it did not prove possible to achieve a good fit to the data at low q values due to the irregular shape and large size distribution of grains in the films (as can be seen from the SEM images of nominally identical films presented in **Figure 4**). Nevertheless, whilst a quantitative analysis has not been possible, we show below that a qualitative analysis can still provide useful information on the evolution of the film during the annealing process.

The evolution of the GISAXS scattering intensity in q_y during thermal annealing at 80 °C is shown in Figure 3a. It can be seen that for annealing times longer than around 60 min, we observe an increase in intensity at lower q values although the shape of the profile remains quite similar throughout the process. By plotting the data in terms of the change in scattering intensity relative to that recorded at $t = 0$ min, it is possible to more easily observe changes in the scattering profile as a function of time during thermal annealing as shown in Figure 3b. It can be seen that during the first 30 min of annealing, the intensity at all q values is slightly lower than that observed at $t = 0$, and that no clear features can be identified. At $t > 40$ min, we observe a gradual increase in intensity at q values below ≈0.02 Å^{-1}, corresponding to length scales greater than ≈30 nm. This increase in intensity gradually manifests itself as a peak in the profile centered at ≈0.005 Å^{-1}, corresponding to a length scale of ≈130 nm. Note that the lower bound of our data is at $q = 1.54 \times 10^{-3}$ Å^{-1}, corresponding to a length scale of ≈400 nm. Our measurements thus suggest that as the perovskite is formed from the crystalline precursor phase, there is an increase in the fraction and number of structures within the film having length scales in the range 30–400 nm, and in particular an increase in the number of structures having length scales between 100 and 150 nm.

Plotting the logarithm of scattering intensity against q^2 at low q values (Guinier analysis) allows for further qualitative analysis.[45] This is shown for q_y in Figure 3c, while Figure 3d presents a similar plot for q_z (taken at $q_y = 0.003$ Å^{-1}). As the annealing process proceeds, the slope of the curve close to $q_y = 0$ (Figure 3c) decreases, attributable to a decrease in the average (lateral) diameter of the scatterers in the film. Similarly, an increase in the slope after the Yoneda peak in q_z, as seen in Figure 3d, indicates an increase in the average height of the grains. Taken together, these observations suggest a change in the aspect ratio of crystal grains during the annealing and transformation process. Finally, the shift of the Yoneda peak toward larger q_z values can be attributed to an increase in the average density of the film.

In order to further investigate these changes in length scales, we have used SEM and atomic force microscopy (AFM) to image nominally identical films that have been annealed

DOI: 10.1002/adfm.201601309

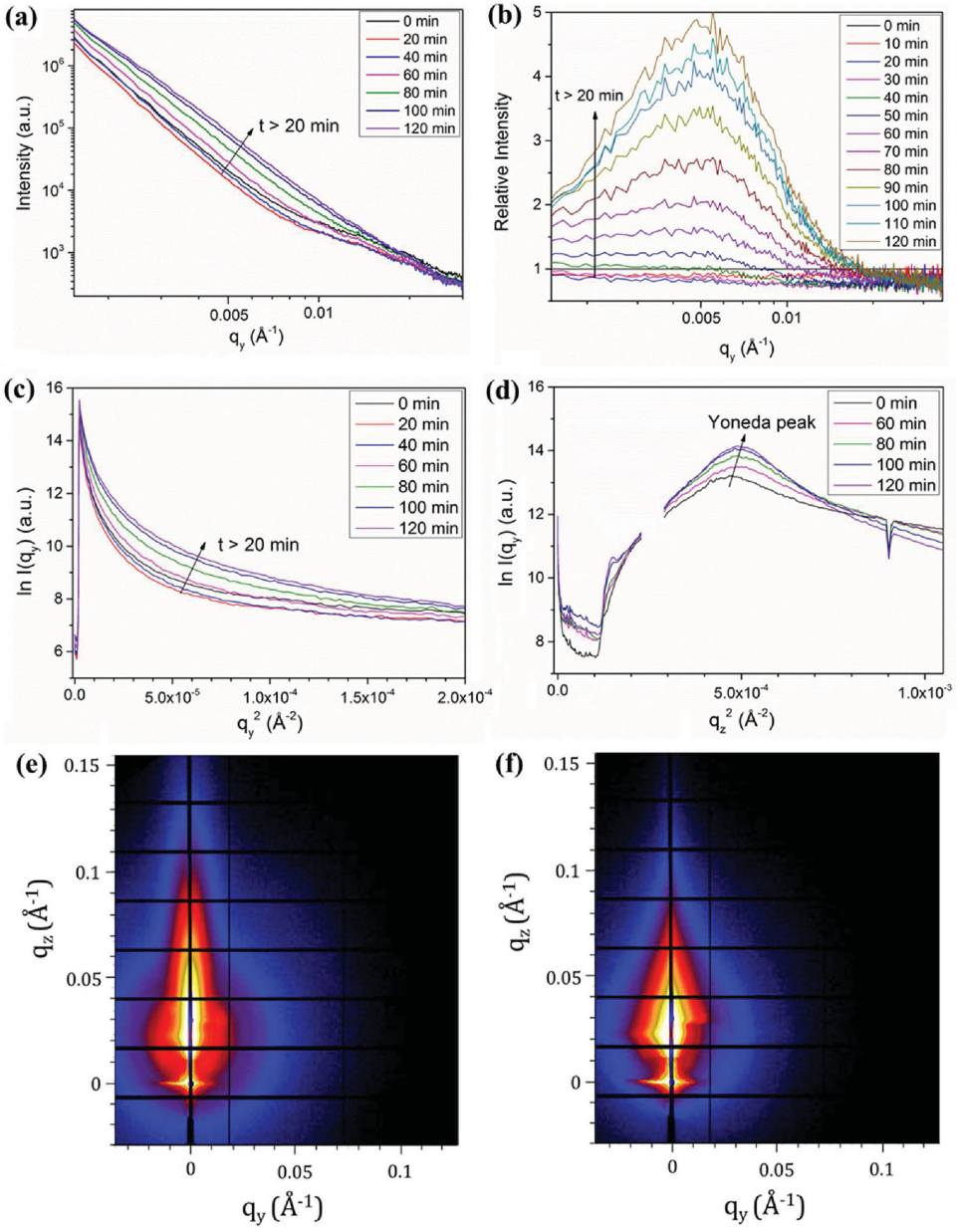

Figure 3. a) Evolution of the GISAXS data slice in q_y during an 80 °C thermal anneal and b) the same data presented as a relative intensity as compared to the data at 0 min. c,d) The Guinier analysis for data slices in q_y and q_z is shown respectively in parts (c) and (d). e,f) Detector data for 0 and 120 min; the slight shading on the right side of the feature is due to shading from the beam-stop, data were thus taken from the left side of the feature.

at 80 °C for various lengths of time. Here we emphasize that while SEM and AFM measurements probe only the surface of the sample, the GISAXS measurements presented above probe the bulk of the film since all measurements are made above the critical angle for the samples. From the SEM images presented in Figure 4, it can be seen that as the annealing time is increased from 60 to 120 min, the film evolves from a structure that is dominated by micron-sized grains separated by voids to one composed of many features at smaller length scales (hundreds of nanometers). At annealing times longer than 120 min, the film morphology appears to stabilize and remains comparatively unchanged following further annealing. The decrease in the apparent diameter of the grains and the significant increase in the fraction of grains having length scales of hundreds of nanometers during the period from t = 60 to 120 min is consistent with the GISAXS data described above. Further SEM images demonstrating this evolution in film morphology are shown in Figure S5 (Supporting Information). Atomic force microscopy images of the perovskite surface, as shown in Figures S6 and S7 (Supporting Information), further confirm such an evolution in lengths scales within the perovskite film during annealing.

The change in length scales around t = 60–120 min is accompanied by an increase in the film surface coverage from ≈80%

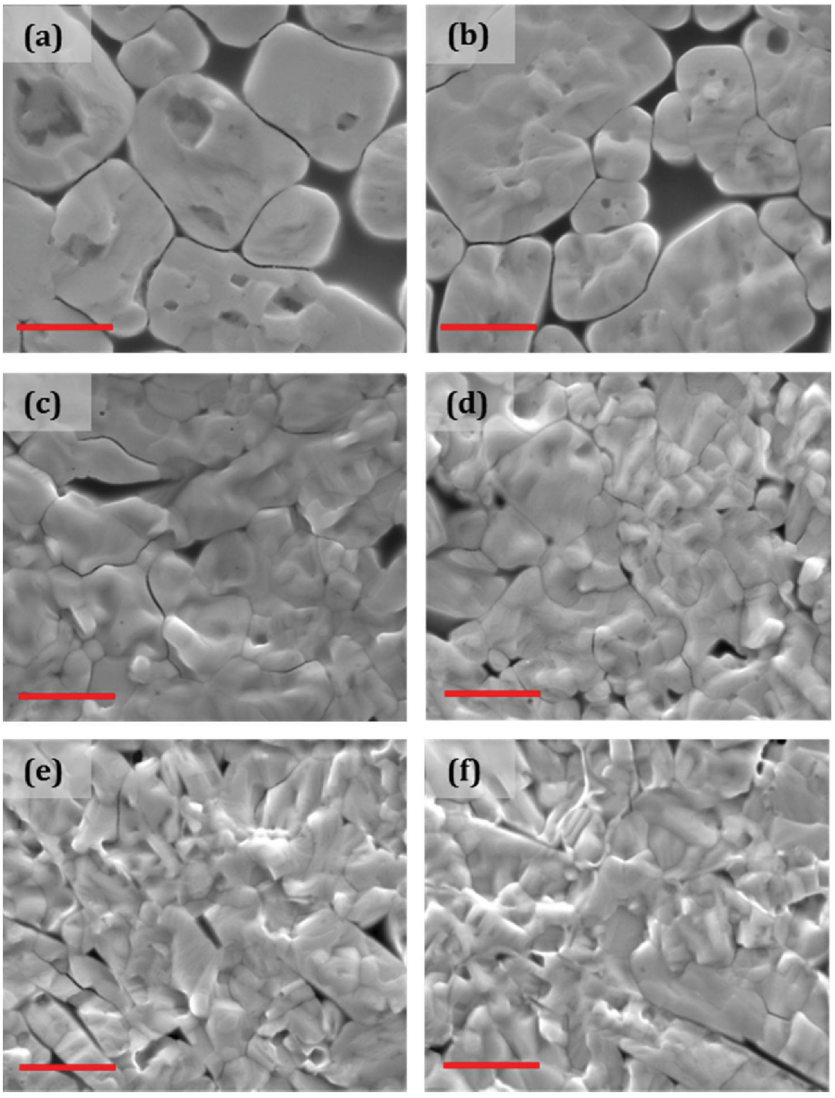

Figure 4. Scanning electron microscopy images of films annealed for periods of a) 60 min, b) 80 min, c) 100 min, d) 120 min, e) 140 min, and f) 180 min. Red scale bars correspond to 1 μm.

to ≈95%, which is consistent with the shift of the Yoneda peak toward larger q_z values. This process is of particular importance due to the necessity of high surface coverage for the fabrication of high performance solar cells. Low surface coverage due to large voids in the perovskite film leads to losses in solar cell efficiency due to both reduced light absorption (reduced short circuit current density, J_{SC}) and additional leakage paths resulting in a reduction in shunt resistance (reduced open circuit voltage, V_{OC} and fill factor, FF).[9,46] The evolution of the film to the more continuous morphology as observed at longer annealing times appears to be linked to the change in length scales as evidenced by the GISAXS data. In particular, the largest changes in GISAXS data and observed film morphology both occur in the period from t = 60–120 min. We speculate that this evolution is critical in the formation of continuous and uniform films, with such properties being necessary in high performance PSC devices prepared using a one-step process.

2.3. The Role of Annealing Treatment on Device Efficiency

In order to correlate solar cell performance with the evolution of perovskite films during the annealing process, films that were nominally identical to those used for the X-ray scattering measurements were fabricated into complete perovskite solar cells having the structure ITO/PEDOT:PSS/$CH_3NH_3PbI_{3-x}Cl_x$/$PC_{70}BM$/Ca/Al. Note we can confidently relate the structures studied using GIWAXS and GISAXS to the device studies presented here, as in all cases the perovskite layer was prepared on a PEDOT:PSS coated substrate. In particular, films prepared for GIWAXS measurements were fabricated on Si/SiO_2/PEDOT:PSS substrates, while films studied using GISAXS measurements and fabricated into devices were fabricated on glass/ITO/PEDOT:PSS substrates. The relative humidity during film preparation and measurements using GIWAXS, GISAXS, and device fabrication was 40%–45%, 45%–50%, and ≈45% respectively. Perovskite films were annealed at 80 °C for varying lengths of time from 80 to 180 min. Device metrics for the resulting solar cells are presented in **Table 1**, with current-density against voltage plots for typical devices prepared using each annealing condition shown in **Figure 5**a. For completeness, we plot histograms showing the spread of device performance for each annealing condition in Figure S8 (Supporting Information). It was found that films annealed for times less than 80 min could be seen by eye to not have fully converted to a perovskite and are thus expected to exhibit poor device performance as well as limited device lifetime. As the annealing time increased from 80 to 100 and then 120 min, the average device PCE increased from 7.8% to 10.7% and finally to 12.2%. This improved efficiency arises due to an increase in J_{SC} from 15.8 to 17.2 and finally to 18.4 mA cm^{-2}, as well as an increase in FF from 50.6 to 64.0 and then 68.8%. At annealing times longer than 120 min, PSC performance begins to reduce with all device metrics undergoing a reduction. Our high efficiency devices exhibit minimal hysteresis in their current density against voltage behavior, as can be seen in Figure S9 (Supporting Information). The observed trends in device performance can be understood with reference to the GISAXS, GIWAXS, and SEM data presented above. Initial increases in performance can be attributed to the combined effect of two processes. First, the increased annealing time leads to an increase in surface coverage, resulting in an enhanced J_{SC} and FF. Concurrently we observe a more complete conversion of precursor materials to the perovskite, and indeed the maximum efficiency of devices corresponds closely to the annealing time (117 min) at which the integrated intensity of

DOI: 10.1002/adfm.201601309

Table 1. Solar cell performance for devices fabricated via an 80 °C thermal anneal for lengths of time from 80–180 min.

Anneal time [min]	PCE [%]	J_{SC} [mA cm^{-2}]	V_{OC} [V]	FF [%]
80	7.8 ± 1.0 (9.2)	15.8 ± 0.9	0.979 ± 0.006	50.6 ± 3.7
100	10.7 ± 0.5 (11.3)	17.2 ± 0.3	0.972 ± 0.004	64.0 ± 3.0
120	12.2 ± 0.3 (12.7)	18.4 ± 0.1	0.966 ± 0.004	68.8 ± 1.2
140	11.9 ± 0.2 (12.2)	18.3 ± 0.1	0.951 ± 0.005	68.4 ± 0.7
180	8.8 ± 0.5 (9.4)	17.5 ± 0.2	0.893 ± 0.012	56.7 ± 3.2

the $q \approx 1$ Å^{-1} GIWAXS diffraction peak takes its maximum value. This correspondence is confirmed in Figure 5b, where we present PCE and the transformed fraction of material [$x(t)$], determined by tracking the integrated intensity of the $q \approx 1$ Å^{-1} diffraction peak as a function of annealing time (see the Supporting Information). Finally, at long annealing times the perovskite begins to undergo a decomposition into various products including lead iodide, as observed via the in situ GIWAXS data, leading to a reduction in device performance, as might be expected.

3. Conclusion

We have applied a variety of in situ and ex situ techniques to observe the formation of $CH_3NH_3PbI_{3-x}Cl_x$ from a precursor film during a thermal annealing step. The activation energy of this transformation has been calculated to be 85 kJ mol^{-1}, a value in line with a previous measurement. Preferential orientation for precursor and perovskite crystallites in the out-of-plane direction is observed throughout the annealing process. In situ GISAXS measurements show that during a thermal anneal at 80 °C, there is an evolution in length scales within the film, with a large increase in features having sizes in the range 30–400 nm. This evolution in length scales is correlated with an increase in film surface coverage, which is known to lead to improved device efficiency. Finally, devices with an average efficiency of 12.2% have been fabricated for nominally identical films having high surface coverage due to an optimization of the annealing time.

4. Experimental Section

Materials: A solution of MAI:$PbCl_2$ (3:1 molar ratio) at 40 wt% in DMF was used (Ossila Ltd. ink I101) for all film fabrication.

Preparation of Substrates and Films: Substrates were cleaned by sequential sonication in warm Helmanex, DI water, and isopropyl alcohol (IPA) before being rinsed in deionised (DI) water and dried with compressed nitrogen. A PEDOT:PSS (poly(3,4-ethylenedioxythiophene) polystyrene sulfonate) (Ossila Ltd.) layer was then spin-coated at 5000 rpm and annealed at 120 °C for 30 min before use, resulting in a layer with thickness ≈30 nm as measured by surface profilometry. The perovskite solution was deposited via spin-coating at 4000 rpm in a one-step process. Here, the precursor solution was held on a 90 °C hotplate for ≥10 min before deposition, with substrates placed on a 90 °C hotplate for ≈5 min before deposition and then transferred immediately to the spin-coater for film casting.

GIWAXS: Experiments were performed at the XMaS beamline at the European Synchrotron Radiation Facility (ESRF), Grenoble, France. Beam energy was 10 keV and the incident angle was 0.24°. Relative humidity was 40%–45% during the experiments. A custom made annealing chamber was mounted on a six circle Huber diffractometer. A 2D MAR detector was mounted on the diffractometer arm with calibration performed by scanning the detector vertically and horizontally and tracking the direct beam position.[47] Perovskite films were spin-cast onto Si/SiO_2/PEDOT:PSS substrates and immediately transferred to the experimental chamber. There was approximately a 2 min delay between spin-coating and the acquisition of the first image on the cold hotplate ($t = 0$). After acquisition of the initial image the hotplate temperature was subsequently raised to the desired value. The hotplate experienced an overshoot when heating (by ≈10 °C), with its measured temperature exceeding the target temperature within 1 min in the 80 °C and 90 °C cases and within 2 min in the 110 °C case. In all cases the temperature dropped to its intended temperature within 10 min of the acquisition of the first image. Further details on how this has been accounted for in the determination of activation energy are given in the Supporting Information. Image processing and analysis was performed using the GI-XRD-GUI program.[47]

GISAXS: Experiments were performed at the I22 beamline at the Diamond Light Source, Didcot, England. Here, the beam energy was set at 12.4 keV and was incident on the sample at an angle of 0.2°. Scattered X-rays were then detected using a Pilatus P3-2M detector. For measurement, perovskite films were spin-cast onto glass/ITO/PEDOT:PSS substrates before being transferred to the hotplate which was already held at the desired temperature. There was approximately a 90 s delay between spin-coating and the acquisition of the first image ($t = 0$). The relative humidity in the lab was measured at 45%–50%. In order to minimize exposure of the sample to X-rays, a fast shutter was used whereby the sample was only exposed to the beam during measurements (corresponding to a 5 s exposure once every 5 min).

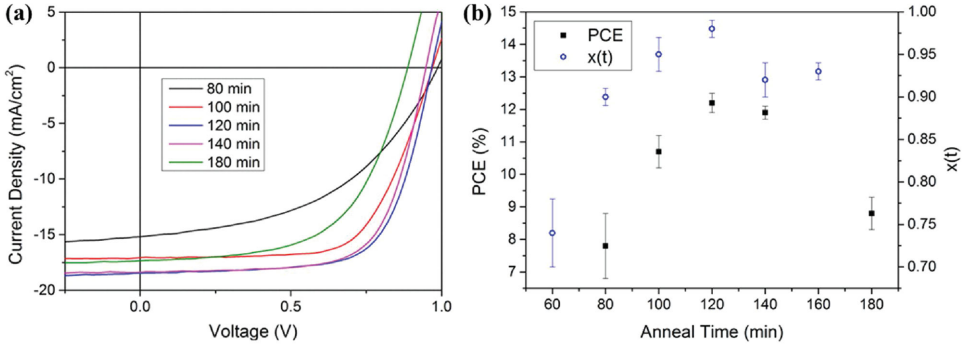

Figure 5. a) Current-density against voltage curves for typical devices fabricated via an 80 °C thermal anneal for various lengths of time between 80 and 180 min. b) PCE and $x(t)$ (defined as normalized integrated intensity of the $q \approx 1$ Å^{-1} diffraction peak determined via GIWAXS data, see the Supporting Information) as a function of annealing time at 80 °C.

Calibration was performed using a collagen sample. Image processing and analysis were performed using the DAWN software package.[48] Data slices in q_y were taken at the Yoneda Peak for each image, and were an average of nine pixels in q_z in order to improve measurement statistics.

Film Characterization: SEM images were taken using an FEI Inspect F scanning electron microscope. Here an incident beam energy of 5 kV was used in combination with a secondary electron detector. AFM measurements were performed using a Veeco Dimension 3100 in tapping mode with Budget Sensors Tap300-G tips. Gwyddion software (http://gwyddion.net/) was used for image analysis.

Fabrication of Solar Cells: Prepatterned glass-ITO substrates were purchased from Ossila Ltd. Substrate cleaning and deposition of the PEDOT:PSS hole transport layer and perovskite active layer were as described above, with perovskite films formed having a thickness of ≈380 nm. Following the thermal annealing step, the perovskite films were moved into a nitrogen glovebox where $PC_{70}BM$ (99%, Ossila Ltd) was deposited by spin-coating of a 50 mg mL^{-1} solution in chlorobenzene (heated for 12 h at 70 °C and filtered using a 0.45 µm PTFE filter) at 1000 rpm, creating a layer having a thickness of ≈120 nm. Devices were then completed with 5 nm Ca and 100 nm Al cathode deposited by evaporation, before being encapsulated using UV epoxy and a glass slide. Three separate substrates were fabricated for each condition with each substrate comprising of four devices, giving a total of 12 devices per condition.

Device Characterization: Current–voltage characteristics were measured in ambient conditions using a Newport 92251A-1000 solar simulator (AM1.5 spectrum at an intensity of 100 mW cm^{-2}). JV scans between 1 and −1 V were measured at a scan rate of 0.5 Vs^{-1}, with no light soaking or prebiasing used before measuring current–voltage characteristics. An aperture mask of 0.025 cm^2 was used to define the device area. The efficiency of the best 50% of devices was reported, thus excluding pixels containing a significant defect whilst avoiding the use of a statistical method that is open to user bias.

Supporting Information

Supporting Information is available from the Wiley Online Library or from the author.

Acknowledgements

The authors thank Darren Watters at Ossila Ltd. for solution preparation, Mejd Alsari and Oier Bikondoa for assistance with the GIWAXS beamtime at ESRF and Bailey Curzadd for construction of the chamber for GIWAXS experiments. The authors also thank Yiwei Zhang, Paul Staniec, and Jon Griffin for assistance with the GISAXS beamtime at Diamond. A.T.B. thanks the EPSRC for funding via the E-Futures Doctoral Training Centre in Interdisciplinary Energy Research EP/G037477/1. The authors gratefully acknowledge funding via UK EPSRC via research grants EP/M025020/1 "High resolution mapping of performance and degradation mechanisms in printable photovoltaic devices" and EP/J017361/1 "Supergen Supersolar Hub."

Received: March 14, 2016
Published online: May 26, 2016

[1] A. Kojima, K. Teshima, T. Miyasaka, Y. Shirai, presented at 210th *Electrochemical Society Meeting*, Cancun, Mexico, Oct–Nov **2006**.
[2] A. Kojima, K. Teshima, Y. Shirai, T. Miyasaka, *J. Am. Chem. Soc.* **2009**, *131*, 6050.
[3] H.-S. Kim, C.-R. Lee, J.-H. Im, K.-B. Lee, T. Moehl, A. Marchioro, S.-J. Moon, R. Humphry-Baker, J.-H. Yum, J. E. Moser, M. Grätzel, N.-G. Park, *Sci. Rep.* **2012**, *2*, 591.
[4] M. M. Lee, J. Teuscher, T. Miyasaka, T. N. Murakami, H. J. Snaith, *Science* **2012**, *338*, 643.
[5] M. A. Green, K. Emery, Y. Hishikawa, W. Warta, E. D. Dunlop, *Prog. Photovoltaics Res. Appl.* **2015**, *23*, 805.
[6] A. Barrows, A. Pearson, C. Kwak, A. Dunbar, A. Buckley, D. Lidzey, *Energy Environ. Sci.* **2014**, *7*, 2944.
[7] A. Mei, X. Li, L. Liu, Z. Ku, T. Liu, Y. Rong, M. Xu, M. Hu, J. Chen, Y. Yang, M. Gratzel, H. Han, *Science* **2014**, *345*, 295.
[8] D. Vak, K. Hwang, A. Faulks, Y.-S. Jung, N. Clark, D.-Y. Kim, G. J. Wilson, S. E. Watkins, *Adv. Energy Mater.* **2015**, *5*, 1401539.
[9] M. Liu, M. B. Johnston, H. J. Snaith, *Nature* **2013**, *501*, 395.
[10] T. M. Schmidt, T. T. Larsen-olsen, J. E. Carlé, D. Angmo, F. C. Krebs, *Adv. Energy Mater.* **2015**, *10*, 1500569.
[11] M. Ramesh, K. M. Boopathi, T.-Y. Huang, Y.-C. Huang, C.-S. Tsao, C.-W. Chu, *ACS Appl. Mater. Interfaces* **2015**, *7*, 2359.
[12] K. Jiang, S.-G. Li, M. Su, X. Cui, J.-H. Huang, Q.-Q. Zhang, X. Zhou, L.-M. Yang, Y. Song, *J. Mater. Chem. A* **2015**, *3*, 9092.
[13] J. Burschka, N. Pellet, S.-J. Moon, R. Humphry-Baker, P. Gao, M. K. Nazeeruddin, M. Grätzel, *Nature* **2013**, *499*, 316.
[14] Z. Xiao, B. Cheng, Y. Shao, Q. Dong, Q. Wang, Y. Yongbo, C. Wang, Y. Gao, J. Huang, *Energy Environ. Sci.* **2014**, *7*, 2619.
[15] C.-G. Wu, C.-H. Chiang, Z.-L. Tseng, *J. Mater. Chem. A* **2014**, *2*, 15897.
[16] F. Hao, C. C. Stoumpos, Z. Liu, R. P. H. Chang, M. G. Kanatzidis, *J. Am. Chem. Soc.* **2014**, *136*, 16411.
[17] H. Zhou, Q. Chen, G. Li, S. Luo, T.-B. Song, H.-S. Duan, Z. Hong, J. You, Y. Liu, Y. Yang, *Science* **2014**, *345*, 542.
[18] W. Zhang, M. Saliba, D. T. Moore, S. Pathak, M. Horantner, T. Stergiopoulos, S. D. Stranks, G. E. Eperon, J. A. Alexander-Webber, A. Abate, A. Sadhanala, S. Yao, Y. Chen, R. H. Friend, L. A. Estroff, U. Wiesner, H. J. Snaith, *Nat. Commun.* **2015**, *6*, 6142.
[19] J. H. Heo, H. J. Han, D. Kim, T. K. Ahn, S. H. Im, *Energy Environ. Sci.* **2015**, *8*, 1602.
[20] J. H. Heo, D. H. Song, H. J. Han, S. Y. Kim, J. H. Kim, D. Kim, H. W. Shin, T. K. Ahn, C. Wolf, T.-W. Lee, S. H. Im, *Adv. Mater.* **2015**, *27*, 3424.
[21] W. S. Yang, J. H. Noh, N. J. Jeon, Y. C. Kim, S. Ryu, J. Seo, S. I. Seok, *Science* **2015**, *348*, 1234.
[22] H.-C. Liao, C.-S. Tsao, M.-H. Jao, J.-J. Shyue, C.-P. Hsu, Y.-C. Huang, K.-Y. Tian, C.-Y. Chen, C.-J. Su, W.-F. Su, *J. Mater. Chem. A* **2015**, *3*, 10526.
[23] T. Miyadera, Y. Shibata, T. Koganezawa, T. N. Murakami, T. Sugita, N. Tanigaki, M. Chikamatsu, *Nano Lett.* **2015**, *15*, 5630.
[24] K. W. Tan, D. T. Moore, M. Saliba, H. Sai, L. A. Estroff, T. Hanrath, H. J. Snaith, U. Wiesner, T. A. N. E. T. Al, *ACS Nano* **2014**, *8*, 4730.
[25] D. T. Moore, H. Sai, K. W. Tan, D. Smilgies, W. Zhang, H. J. Snaith, U. Wiesner, L. A. Estroff, *J. Am. Chem. Soc.* **2015**, *137*, 2350.
[26] E. L. Unger, A. R. Bowring, C. J. Tassone, V. L. Pool, A. Gold-parker, R. Cheacharoen, K. H. Stone, E. T. Hoke, M. F. Toney, M. D. Mcgehee, *Chem. Mater.* **2014**, *26*, 7158.
[27] J. Schlipf, P. Docampo, C. J. Schaffer, V. Körstgens, L. Bießmann, F. C. Hanusch, N. Giesbrecht, S. Bernstorff, T. Bein, P. Muller-Buschbaum, *J. Phys. Chem. Lett.* **2015**, *6*, 1265.
[28] K. Liang, D. B. Mitzi, M. T. Prikas, *Chem. Mater.* **1998**, *10*, 403.
[29] K. Wu, A. Bera, C. Ma, Y. Du, Y. Yang, L. Li, T. Wu, *Phys. Chem. Chem. Phys.* **2014**, *16*, 22476.
[30] T. Baikie, Y. Fang, J. M. Kadro, M. Schreyer, F. Wei, S. G. Mhaisalkar, M. Graetzel, T. J. White, *J. Mater. Chem. A* **2013**, *1*, 5628.
[31] H. Yu, F. Wang, F. Xie, W. Li, J. Chen, N. Zhao, *Adv. Funct. Mater.* **2014**, *24*, 7102.
[32] M. I. Dar, N. Arora, P. Gao, S. Ahmad, M. Grätzel, M. K. Nazeeruddin, *Nano Lett.* **2014**, *14*, 6991.
[33] A. Dualeh, N. Tétreault, T. Moehl, P. Gao, M. K. Nazeeruddin, M. Grätzel, *Adv. Funct. Mater.* **2014**, *24*, 3250.

[34] S. Colella, E. Mosconi, P. Fedeli, A. Listorti, F. Gazza, F. Orlandi, P. Ferro, T. Besagni, A. Rizzo, G. Calestani, G. Gigli, F. De Angelis, R. Mosca, *Chem. Mater.* **2013**, *25*, 4613.
[35] S. Lilliu, T. Agostinelli, E. Verploegen, E. Pires, M. Hampton, M. Al-Hashimi, M. J. Heeney, M. F. Toney, J. Nelson, J. E. Macdonald, *Macromol. Rapid Commun.* **2011**, *32*, 1454.
[36] W. Huang, F. Huang, E. Gann, Y. Cheng, C. R. Mcneill, *Adv. Funct. Mater.* **2015**, *25*, 5529.
[37] Y.-C. Huang, C.-S. Tsao, Y.-J. Cho, K.-C. Chen, K.-M. Chiang, S.-Y. Hsiao, C.-W. Chen, C.-J. Su, U.-S. Jeng, H.-W. Lin, *Sci. Rep.* **2015**, *5*, 13657.
[38] M. Saliba, K. W. Tan, H. Sai, D. T. Moore, T. Scott, W. Zhang, L. A. Estroff, U. Wiesner, H. J. Snaith, *J. Phys. Chem. C* **2014**, *118*, 17171.
[39] S. T. Williams, F. Zuo, C.-C. Chueh, C.-Y. Liao, P.-W. Liang, A. K.-Y. Jen, *ACS Nano* **2014**, *8*, 10640.
[40] O. Malinkiewicz, C. Roldán-Carmona, A. Soriano, E. Bandiello, L. Camacho, M. K. Nazeeruddin, H. J. Bolink, *Adv. Energy Mater.* **2014**, *4*, 1400345.
[41] E. Edri, S. Kirmayer, A. Henning, S. Mukhopadhyay, K. Gartsman, Y. Rosenwaks, G. Hodes, D. Cahen, *Nano Lett.* **2014**, *14*, 1000.
[42] J. Xiong, B. Yang, R. Wu, C. Cao, Y. Huang, C. Liu, Z. Hu, H. Huang, Y. Gao, J. Yang, *Org. Electron.* **2015**, *24*, 106.
[43] P. Löper, M. Stuckelberger, B. Niesen, J. Werner, M. Filipič, S.-J. Moon, J.-H. Yum, M. Topič, S. De Wolf, C. Ballif, *J. Phys. Chem. Lett.* **2015**, *6*, 66.
[44] Y. Yoneda, *Phys. Rev.* **1963**, *131*, 2010.
[45] G. Renaud, R. Lazzari, F. Leroy, *Surf. Sci. Rep.* **2009**, *64*, 255.
[46] G. E. Eperon, V. M. Burlakov, P. Docampo, A. Goriely, H. J. Snaith, *Adv. Funct. Mater.* **2014**, *24*, 151.
[47] S. Lilliu, T. Agostinelli, E. Pires, M. Hampton, J. Nelson, J. E. Macdonald, *Macromolecules* **2011**, *44*, 2725.
[48] M. Basham, J. Filik, M. T. Wharmby, P. C. Y. Chang, B. El Kassaby, M. Gerring, J. Aishima, K. Levik, B. C. A. Pulford, I. Sikharulidze, D. Sneddon, M. Webber, S. S. Dhesi, F. Maccherozzi, O. Svensson, S. Brockhauser, G. Náray, A. W. Ashton, *J. Synchrotron Radiat.* **2015**, *22*, 853.